Draft version January 4, 2022
Typeset using LaTeX **twocolumn** style in AASTeX631

The vertical Fermi and eROSITA bubbles inclined jets: A proof-of-concept study

Po-Hsun Tseng [1] H.-Y. Karen Yang [2] Hsi-Yu Schive [1,3,4,5] and Tzihong Chiueh [1,3,4]

[1] *Institute of Astrophysics, National Taiwan University, Taipei 10617, Taiwan*
[2] *Institute of Astronomy and Department of Physics, National Tsing Hua University, Hsinchu 30013, Taiwan*
[3] *Department of Physics, National Taiwan University, Taipei 10617, Taiwan*
[4] *Center for Theoretical Physics, National Taiwan University, Taipei 10617, Taiwan*
[5] *Physics Division, National Center for Theoretical Sciences, Taipei 10617, Taiwan*

ABSTRACT

1. Release the caveat of jet direction.
2. Rule out the hadronic process.
3. Predict the small inner bubbles.
4. How to explain why we assume e_CR ■ e_gas
5. How to explain the lifespan of bubbles is too long.
6. How to explain the jet power.
7. How to explain the inconsistant of gamma-ray map.

Keywords: keywords

1. INTRODUCTION

Early attempts to model the Fermi bubbles assumed that the jet is vertial to the Galactic plane...

2. METHODOLOGY

We used the GPU-accelerated special relativistic hydrodynamics AMR code (GAMER-SR) developed at the National Taiwan University (Schive et al. 2010, 2018; Tseng et al. 2021) to carry out the simulations of the Fermi and eROSITA bubbles by CR and relativistic fluid injections from the GC.

The CRs are advected with the thermal gas, and in return the velocities of gas can react to the gradients of the CR pressure via the source term containing spatial divergence of fluid velocities.

Although the high-energy CRe (10 — 100 GeV) plays a crucial role in reproducing the γ-ray map within the range of 1 — 100 GeV, we assume the pressure of CRe is much less than that of gas throughout the simulation so that we , and the Fermi bubbles can be outlined against the eROSITA bubbles.

As stressed by Yang et al. (2012), CR diffusion has insignificant effect on the overall morphology of the Fermi bubbles, but only sharpens the edges of the simulated bubbles by the interplay between anisotropic CR diffusion and magnetic fields with suppressed perpendicular diffusion across the bubble surface. Moreover, the bubbles should be weak due to adiabatic expansion, and thus the magnetic fields has little effect on the overall dynamics. For these two reasons, we have ignored the CR diffusion and the magnetic field throughout the simulation.

We do not simulate the spectral evolution of the CR, and we neglected the cooling and heating processes of CRs, such as energy losses due to synchrotron and inverse Compton emission, and reacceleration in shocks.

In this approach, we treat CRs as a single species without distinction between electrons and protons, that cannot react to the gas via the application of CRe

Corresponding author: Po-Hsun Tseng
zengbs@gmail.com

pressure, and solve directly for the evolution of CR energy density $e_{\rm cr}$ as a function of $\mathbf{r}$ and t.

Since the relativistic fluid ejected by the jet source is quickly stalled off and slowed down by a dense ISM disk in a short time, and the relativistic fluid accounts for a little minority of total mass inside the simulation box, we still use the Newtonian gravity to attack this problem.

The governing equations solving the special relativistic ideal fluid including CR advection, and dynamical coupling between the thermal gas and CRs without CR diffusion can be written a succinct form as

$$\partial_t D + \partial_j \left(D U^j / \gamma \right) = 0, \tag{1a}$$

$$\partial_t M^i + \partial_j \left(M^i U^j / \gamma + p_{\rm gas} \delta^{ij} \right) = -\rho \partial_i \Phi, \tag{1b}$$

$$\partial_t \tilde{E} + \partial_j \left[\left(\tilde{E} + p_{\rm gas} \right) U^j / \gamma \right] = 0, \tag{1c}$$

$$\partial_t \left(\gamma e_{\rm cr} \right) + \partial_j \left(e_{\rm cr} U^j \right) = -p_{\rm cr} \partial_j U^j, \tag{1d}$$

where the five conserved quantities of gas D, M^i, and $\tilde{E}$ are the mass density, the momentum densities, and the reduced energy density, respectively. The reduced energy density is defined by subtracting the rest mass energy density of gas from the total energy density of gas. γ and U^j are the temporal and spatial component of four-velocity of gas. ρ is the gas density in the local rest frame defined by D/γ. $p_{\rm gas}$ is the gas pressure. $p_{\rm cr}$ and $e_{\rm cr}$ are the CR pressure and CR energy density measured in the local rest frame. Φ is the gravitation potential. c is the speed of light, and δ^{ij} is the Kronecker delta notation. Throughout this paper, Latin indices run from 1 to 3, except when stated otherwise.

The set of Equation (1) is closed by using the Taub-Mathews equation of state (Taub 1948; Mathews 1971) that approximates the exact EoS (Synge 1957) for ultra-relativistically hot gases coexisting with non-relativistically cold gases.

GAMER-SR adopts a new algorithm (Tseng et al. 2021) to convert between primitive (ρ, U^j, p) and conserved variables (D, M^j, $\tilde{E}$), significantly reducing numerical error caused by catastrophic cancellations that commonly occur within the regions with high Mach number flows. e.g., jet-ISM interaction zones.

GAMER-SR also adaptively and locally reduce the min-mod coefficient (Tseng et al. 2021) within the failed patch group. Doing so provides an elegant way to avoid the use of pressure/density floor, being unnatural but widely used in almost publicly available codes.

2.1. *The Galactic and Disk Models*

As a proof-of-concept study, we approximate conventionally axisymmetric stellar potential of Milky Way by a plane-parallel potential that is symmetric about the mid-plane $z = 0$ in a simulation box size of $14\times14\times28$ kpc, slightly larger than the size of eROISTA bubbles.

The plane-parallel potential is fixed throughout our simulations and given by

$$\Phi_{\rm total}(z) = \Phi_{\rm bulge}(z) + \Phi_{\rm halo}(z), \tag{2}$$

where

$$\Phi_{\rm bulge}(z) = 2\sigma^2_{\rm bulge} \ln\cosh\left(z\sqrt{\frac{2\pi G\rho^{\rm peak}_{\rm bulge}}{\sigma^2_{\rm bulge}}} \right) \tag{3}$$

is the potential of an isothermal slab mainly contributed by stars around the Galactic bulge, and $\Phi_{\rm halo}(z) = v^2_{\rm halo} \ln\left(z^2 + d^2_{\rm h}\right)$ is a plane-parallel dark logarithmic halo potential.

With the help of the isothermal and hydrostatic equilibrium conditions, and assuming the interfaces between isothermal disk and atmosphere are in pressure equilibrium, we can write the steady-state gaseous density distributions, confined in the total potential, of the disk and the Galactic atmosphere as

$$\rho_{\rm isoDisk}(z) = \rho^{\rm peak}_{\rm isoDisk} \exp\left[-\frac{\Phi_{\rm total}(z)}{k_B T_{\rm isoDisk}/m_{\rm p}} \right], \text{ if } |z| < z_0 \tag{4a}$$

$$\rho_{\rm atmp}(z) = \rho^{\rm peak}_{\rm atmp} \exp\left[-\frac{\Phi_{\rm total}(z)}{k_B T_{\rm atmp}/m_{\rm p}} \right], \text{ otherwise,} \tag{4b}$$

where $m_{\rm p}$ is the proton mass, $T_{\rm isoDisk}$ and $T_{\rm atmp}$ is the temperature of the isothermal disk and atmosphere, $\rho^{\rm peak}_{\rm isoDisk}$ and $\rho^{\rm peak}_{\rm atmp}$ is the peak mass density of the disk and atmosphere on the mid-plane $z = 0$.

We tabulate parameters in the first four categories of Table 1, except for $\rho^{\rm peak}_{\rm atmp}$ that can be derived from the other known parameters and pressure equilibrium condition on the interfaces ($z = \pm z_0$) between the disk and atmosphere.

The density profile of Equation (4) is shown in Figure 1 and compared to the observed result (Miller & Bregman 2013) beyond 1 kpc.

Note that there is an difficulty in disentangling the contribution of the Local Bubble, a supernova remnant in which the Solar System is embedded (Snowden et al. 1990), and the contribution from solar wind charge-exchange processes, which produce soft X-ray emission throughout the Solar System. As a result, the density profile of the Galactic halo remains unclear (Bland-Hawthorn & Gerhard 2016).

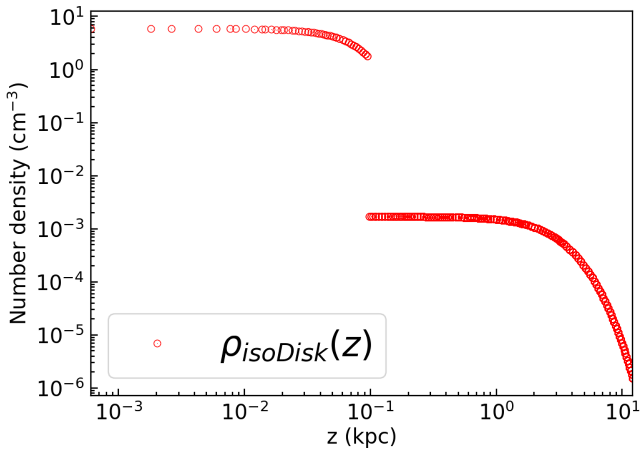

Figure 1. The profile of $\rho_{\rm isoDisk}(z)$ along z-axis.

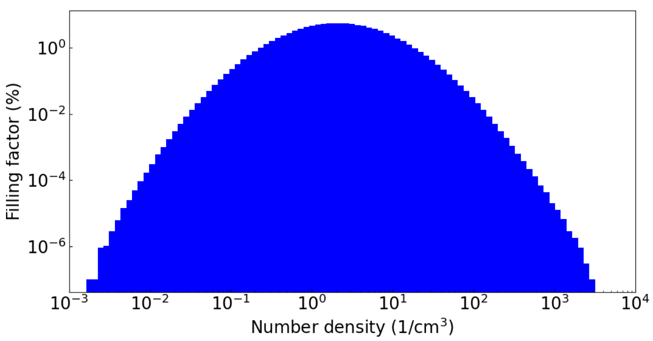

Figure 2. The initial density distribution of the number density for a settling ISM without jet source.

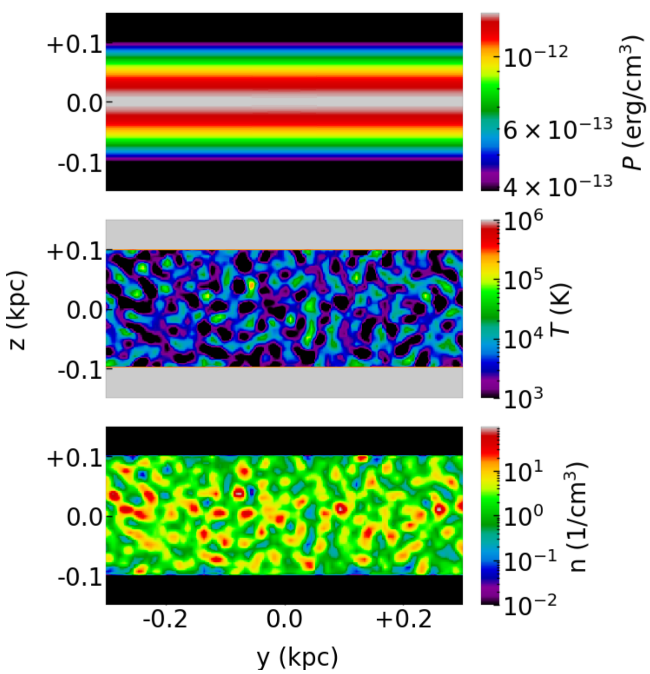

Figure 3. The slice of pressure (top), temperature (middle), and number density (bottom) in the y-z plane passing through the center of the disk.

2.2. *The Clumpy Multiphase Interstellar Medium*

A crucial component in our work is the clumpy ISM disk initialized by the publicly available pyFC code [1].

pyFC randomly generates dimensionless 3D scalar field $f(\mathbf{x})$ that obeys the log-normal probability distribution with mean μ and dispersion σ, and follows the power-law Kolmogorov spectrum

$$D(\mathbf{k}) = \int k^2 \hat{f}(\mathbf{k}) \hat{f}^*(\mathbf{k}) d\Omega \propto k^{-\beta}, \tag{5}$$

where $\hat{f}(\mathbf{k})$ is the Fourier transform of $f(\mathbf{x})$. The spectrum $D(\mathbf{k})$ in the Fourier space is characterized by the power law index $\beta = 5/3$, the Nyquist limit $k_{\rm max}$, and the lower cutoff wave number $k_{\rm min}$. $k_{\rm max}$ is one-half of the spatial resolution within disk, and $k_{\rm min}$ is 375.0, corresponding to the maximum size of an individual clump $\sim$ 20 pc. Lewis & Austin (2002) and Wagner et al. (2012) have outlined a detailed procedure for constructing a clumpy scalar field, and we do not repeat here.

The density of clumpy disk can thus be obtained by taking the scalar products of $f(\mathbf{x})$ with $\rho_{\rm isoDisk}(z)$ over all cells within the disk, i.e., $\rho_{\rm ismDisk}(\mathbf{x}) = f(\mathbf{x})\rho_{\rm isoDisk}(z)$. Also, the pressure equilibrium within the clumpy disk implies that the temperature of disk is $T_{\rm ismDisk}(\mathbf{x}) = T_{\rm isoDisk}(z)\rho_{\rm isoDisk}(z)/\rho_{\rm ismDisk}(\mathbf{x})$.

Table 1 summarize the parameters of the clumpy disk and their references.

On the basis of this setup, we cover the AMR base level with $16 \times 16 \times 32$ root cells, refined progressively on the mid-plane $z = 0$ based on the gradient of mass density. We also restrict the refinement level at 7 within the cold disk so that a molecular cloud can be adequately resolved by approximately 30 cells along their diameter, 20 pc.

2.3. *Inclined jet injection*

Early observation (Gallimore et al. 2006) has proposed that there is a lack of preferred orientation of jets with respect to the plane of the disc. There are a number of galaxies in which the jets are inclined to the disc normal (e.g. NGC 3079, Cecil et al. 2001; NGC 1052, Dopita et al. 2015), including galaxies in which the jets lie in the plane of the disc (e.g. IC 5063, Morganti et al. 2015).

Motivated by these observations, we simulate three cases with different inclined angles, 10°, 45°, and 80° with respect to the Galactic plane in order to release the caveat that the jet direction must be perpendicular to the Galactic plane, and in particular to investigate

[1] https://pypi.python.org/pypi/pyFC

Table 1. Parameters of the disk, atmosphere, and gravitational potential in the simulation.

Parameter	Description	Value	Reference
Static stellar potential			
$\sigma_{\rm bulge}$	Velocity dispersion of bulge	100 km·s^{-1}	(Valenti et al. 2018)
$\rho_{\rm bulge}^{\rm peak}$	Peak average density of bulge	4×10^{-24} g·cm^{-3}	N/A
Static dark halo potential			
$v_{\rm halo}$		131.5 km·s^{-1}	(Johnston et al. 1995)
$d_{\rm h}$	Core radius	12 kpc	"
Atmosphere			
$T_{\rm atmp}$	Temperature of atmosphere	10^6 K	(Tepper-García et al. 2015)
Isothermal disk			
z_0	Scale height of disk	100 pc	(Ferrière 2001)
$T_{\rm isoDisk}$	Temperature of disk	10^3 K	"
$\rho_{\rm isoDisk}^{\rm peak}$	Peak mass density of disk	10^{-23} g·cm^{-3}	"
Clumpy disk			
$T_{\rm c}$	Critical temperature of warm atomic phase	10^4 K	(Ferrière 2001)
† $k_{\rm min}$	Cutoff wave number	375.0	"
μ	Mean of scalar field	1.0	N/A
‡ σ	Dispersion of scalar field	5.0	(Federrath et al. 2010)
β	Power law index	-5/3	N/A

† $k_{\rm min} = 375.0$ leads to the size of an individual molecular cloud ~ 100 pc.
‡ In numerical simulations of turbulence, Federrath et al. (2010) find $\sigma \sim 3.6$ and 35 for solenoidal (divergence-free) and compressive (curl-free) driving force, respectively, so that our adopted value of 5 is closer to their solenoidal result.

the effect of the jet-disk misalignment on the symmetry of bubbles.

All three cases with different inclined angles share the same injection parameters: the density contrast between the thermal gas contained in the jet source and the ambient gas, $\rho_{\rm jet}/\rho_{\rm amb} = 10^{-3}$, the temperature contrast, $T_{\rm jet}/T_{\rm amb} = 2 \times 10^4$, the CR energy density $e_{\rm CR}$ =??, and the flow 4-velocity inside the jet source $\beta\gamma = 0.6$ along the symmetric axis of cylinder. The jet power is thus 3.2×10^{42} erg/s, resulting in the Eddington ratio 0.008.

Note that as we inject the jets at the center of the clumpy disk, we define the ambient gas density by the peak density of the isothermal disk on the mid-plane $z = 0$ (i.e. $\rho_{\rm isoDisk}^{\rm peak}$), as opposed to the *clumpy* density around the jet source, to avoid ambiguous definition.

The bipolar jets are constantly ejected from a cylindrical source with diameter and height of 4 pc, leading to the source volume ~ 50 pc^3 is much smaller than that of individual clump by a factor of 83. By intentionally reducing the volume ratio of the jet source to an individual clump, we can diminish the effect of the randomness of the clumps on the bubbles.

We resolve the jet source with the highest refinement level 11, bringing the finest spatial resolution up to 0.4 pc.

1. Why the overall structure is insensitive to jet direction?
   (a) Jet source size.
   (b) Cold disk.
   (c) Large pressure gradient along z-direction.

3. RESULTS

3.1. *X-ray emission*

Thermal bremsstrahlung: The X-ray emissivity in an energy range 1.4–1.6 keV is calculated using the MEKAL model (Mewe et al. 1985; Kaastra & Mewe 1993; Liedahl et al. 1995) implemented in the utility XSPEC (Arnaud 1996), assuming solar metallicity.

Note that the observed X-ray emission is contributed by all the gas in the Milky Way halo, which likely extends to a radius of ~250 kpc (Blitz & Robishaw 2000; Grcevich & Putman 2009), much bigger than our simulation box. Therefore, we first compute the X-ray emissivity from the simulated gas within a radius of 25 kpc away from the GC. Then, beyond 25 kpc the gas is assumed to be isothermal with $T = 10^6$ K and follows out to a radius of 250 kpc the observed density profile of (Tepper-García et al. 2015).

3.2. *Gamma-ray emission*

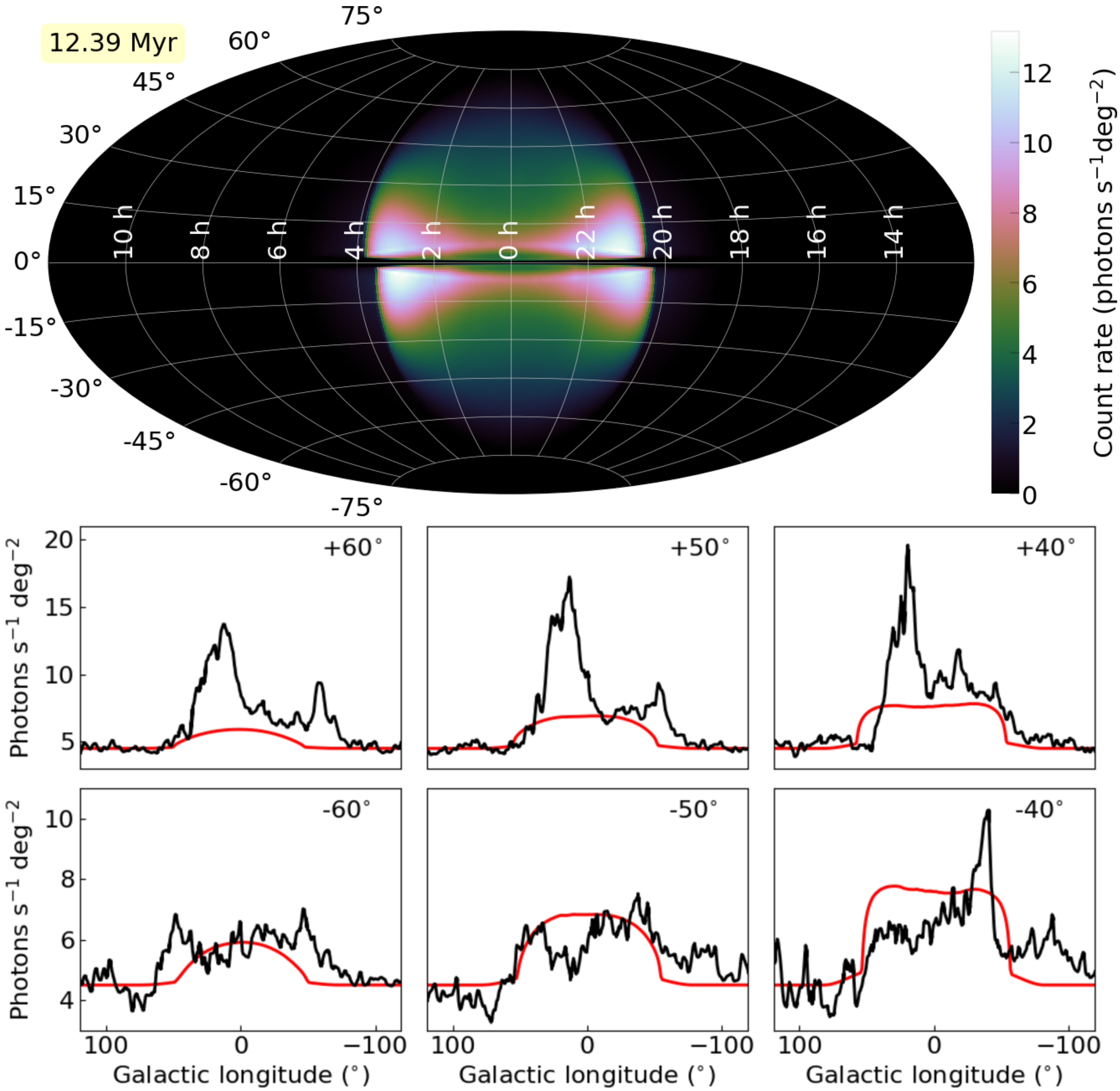

Figure 4. One-dimensional surface-brightness profiles in the same energy band , cut at various galactic latitudes (as labelled). For comparison, we also show ...

3.2.1. *Leptonic process*

In the leptonic scenario, the gamma-rays originate from IC scattering of the ISRF by CRe. The CRe spectrum follows a power law distribution with a spectral index p = 2 and ranges from $m_{\rm e}c^2$ (0.5 MeV) to $10^6 m_{\rm e}c^2$ (0.5 TeV).

The emissivity of the upscattered photons at the energy ϵ_1 is given by the double integrals (Blumenthal & Gould 1970) over the range of incident photon energy and the CRe Lorentz factor:

$$\frac{dE}{dtd\epsilon_1 dV} =$$
$$\frac{3}{4}\sigma_T c\mathbb{C}\epsilon_1 \int_{\epsilon_{\min}}^{\epsilon_{\max}} \frac{n(\epsilon)}{\epsilon} d\epsilon \int_{\gamma_{\min}(\epsilon)}^{\gamma_{\max}} \gamma^{-(p+2)} f(q,\Gamma) d\gamma, \quad (6a)$$

$$f(q,\Gamma) =$$
$$2q\ln q + (1+2q)(1-q) + 0.5(1-q)\frac{(\Gamma q)^2}{1+\Gamma q}, \quad (6b)$$

$$q = \frac{\epsilon_1/\gamma\ m_e c^2}{\Gamma(1-\epsilon_1/\gamma m_e c^2)}, \quad (6c)$$

$$\Gamma = \frac{4\epsilon\gamma}{m_e c^2}, \quad (6d)$$

$$\gamma_{\min}(\epsilon) = 0.5\left(\frac{\epsilon_1}{m_e c^2} + \sqrt{\left(\frac{\epsilon_1}{m_e c^2}\right)^2 + \frac{\epsilon_1}{\epsilon}}\right), \quad (6e)$$

where σ_T is the Thomson cross section, c speed of light, m_e electron mass, $n(\epsilon)$ the photon number density of ISRF per energy, γ the Lorentz factor of CRe, $\mathbb{C}$ and p are the normalization constant and spectral index of CRe power-law spectrum, $\gamma_{\min}(\epsilon)$ is the minimum required Lorentz factor of CRe such that CRe is energetic sufficient for producing scattered photon at the energy ϵ_1 from an incident photon energy ϵ. $\gamma_{\max}$ is the maximum CRe Lorentz factor in the spectrum, i.e. $\gamma_{\max} = 10^6$.

We integrate the incident photon energy from $\epsilon_{\min} = 1.13 \times 10^{-4}$ eV (CMB radiation) to $\epsilon_{\max} = 13.59$ eV (starlight) in order to facilitate a reliable interpretation.

The gamma-ray emissivity is computed for each computational cell in our simulations using the Klein–Nishina IC cross-section (Jones 1968) based on the simulated CR number density and the ISRF model given by Porter et al. (2017).

To evaluate the simulated photon flux I at the energy ϵ_1 and take into account the perspective projection effect, we integrate the emissivity over line-of-sights from the solar position:

$$I = \frac{1}{\epsilon_1}\int \frac{dE}{dtd\epsilon_1 dV} dl. \quad (7)$$

3.2.2. *Hadronic process*

In the hadronic model, CRp undergo hadronic collisions with thermal gas protons and produce γ-ray via pion decay. The volume emissivity of the emission can be written as

$$\epsilon \propto U_{\mathrm{CRp}} n_p \sigma_p \kappa_{pp}. \quad (8)$$

$$\frac{dE}{dtd\epsilon_1 dV} = cn_H pC\left(\frac{\epsilon_1}{m_p c^2}\right)^{-p} \int_0^1 \sigma(\epsilon_p) F(x,\epsilon_p) x^p dx. \quad (9)$$

$$\sigma(\epsilon_p) = 34.3 + 1.88L + 0.25L^2\left[1 - \frac{E_{\mathrm{threshold}}}{E_p}\right]^4 \text{ mb}. \quad (10)$$

$$F(x,\epsilon_p) = B\frac{d}{dx}\left[\ln(x)\left(\frac{1-x^\beta}{1+kx^\beta(1-x^\beta)}\right)^4\right], \quad (11)$$

where $x = \epsilon_1/\epsilon_p$, $B = 1.30 + 0.14L + 0.011L^2$, $\beta = \left(1.79 + 0.11L + 0.008L^2\right)^{-1}$, $\left(0.801 + 0.049L + 0.014L^2\right)^{-1}$, $L = \ln\left(\epsilon_p/1\ \mathrm{TeV}\right)$.

4. TO-DO-LIST

1. Predict cold inner bubbles, emitting OIII or OII spectrum.

5. CONCLUSIONS

DATA AVAILABILITY

The data underlying this article are available in the article and in its online supplementary material.

REFERENCES

Arnaud K. A., 1996, in Jacoby G. H., Barnes J., eds, Astronomical Society of the Pacific Conference Series Vol. 101, Astronomical Data Analysis Software and Systems V. p. 17

Bland-Hawthorn J., Gerhard O., 2016, Annual Review of Astronomy and Astrophysics, 54, 529

Blitz L., Robishaw T., 2000,] 10.1086/309457, 541, 675

Blumenthal G. R., Gould R. J., 1970, Reviews of Modern Physics, 42, 237

Cecil G., Bland-Hawthorn J., Veilleux S., Filippenko A. V., 2001, The Astrophysical Journal, 555, 338

Dopita M. A., et al., 2015, The Astrophysical Journal Supplement Series, 217, 12

Federrath C., Roman-Duval J., Klessen R. S., Schmidt W., Low M.-M. M., 2010, Astronomy and Astrophysics, 512, A81

Ferrière K. M., 2001, Rev. Mod. Phys., 73, 1031

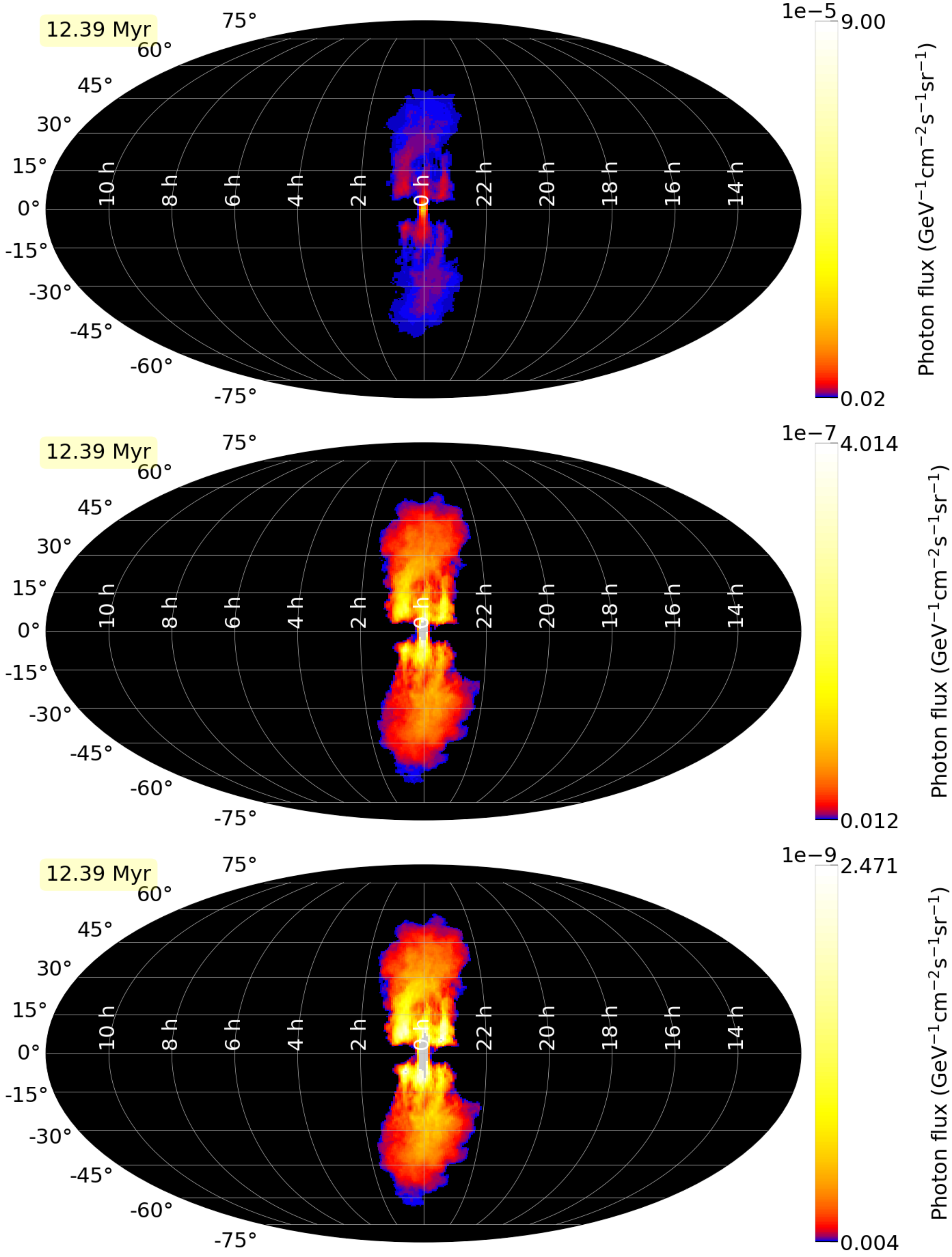

Figure 5. The simulated photon flux at 2 GeV (top), 10 GeV (middle), and 100 GeV (bottom).

Gallimore J. F., Axon D. J., O'Dea C. P., Baum S. A., Pedlar A., 2006, The Astronomical Journal, 132, 546

Grcevich J., Putman M. E., 2009,] 10.1088/0004-637x/696/1/385, 696, 385

Johnston K. V., Spergel D. N., Hernquist L., 1995, The Astrophysical Journal, 451, 598

Jones F. C., 1968, Physical Review, 167, 1159

Kaastra J. S., Mewe R., 1993, A&AS, 97, 443

Lewis G. M., Austin P. H., 2002, 1th Conference on AtmosphericRadiation

Liedahl D. A., Osterheld A. L., Goldstein W. H., 1995, ApJL, 438, L115

Mathews W. G., 1971, ApJ, 165, 147

Mewe R., Gronenschild E. H. B. M., van den Oord G. H. J., 1985, A&AS, 62, 197

Miller M. J., Bregman J. N., 2013, The Astrophysical Journal, 770, 118

Morganti R., Oosterloo T., Oonk J. B. R., Frieswijk W., Tadhunter C., 2015, Astronomy & Astrophysics, 580, A1

Porter T. A., Jóhannesson G., Moskalenko I. V., 2017, The Astrophysical Journal, 846, 67

Schive H.-Y., Tsai Y.-C., Chiueh T., 2010, The Astrophysical Journal Supplement Series, 186, 457

Schive H.-Y., ZuHone J. A., Goldbaum N. J., Turk M. J., Gaspari M., Cheng C.-Y., 2018, Monthly Notices of the Royal Astronomical Society, 481, 4815

Snowden S. L., Cox D. P., McCammon D., Sanders W. T., 1990, The Astrophysical Journal, 354, 211

Synge J. L., 1957, North-Holland Pub. Co.; Interscience Publishers

Taub A. H., 1948, Physical Review, 74, 328

Tepper-García T., Bland-Hawthorn J., Sutherland R. S., 2015, The Astrophysical Journal, 813, 94

Tseng P.-H., Schive H.-Y., Chiueh T., 2021, Monthly Notices of the Royal Astronomical Society, 504, 3298

Valenti E., et al., 2018, A&AS, 616, A83

Wagner A. Y., Bicknell G. V., Umemura M., 2012, The Astrophysical Journal, 757, 136

Yang H.-Y. K., Ruszkowski M., Ricker P. M., Zweibel E., Lee D., 2012, The Astrophysical Journal, 761, 185

APPENDIX